nature communications

Article

https://doi.org/10.1038/s41467-026-70544-7

Extended valley lifetime and giant energy splitting induced by chiral plasmon-valley exciton selective coupling

Received: 10 October 2025

Accepted: 24 February 2026

Published online: 13 March 2026

Check for updates

Jiahe Liu[1,2], Feihong Liu[1], Tingyang Xing[1], Yifan Wang[1], Zhiwei Peng[1], Liang Guo[2], Chen Hu[3,4], Wang Yao[5,6,7], Xiang Zhang[7,8] & Dangyuan Lei[1,9]

The broken inversion symmetry in monolayer transition metal dichalcogenides (TMDs) permits light of specific helicities to address valley-polarized excitonic states, which could serve as inherent information carriers. Achieving large valley energy splitting and long valley lifetimes at room temperature is essential for practical valleytronic applications, yet remains challenging due to strong intervalley interactions. To tackle this, we coupled a single chiral plasmonic nano-resonator with monolayer MoS_2 to prolong the latter's valley polarization through chiral plasmon-valley exciton selective coupling. Our findings show that the selective coupling significantly prolongs the valley exciton population contrast lifetime in the coupled MoS_2, originating from valley energy splitting induced by the selective coupling that breaks the energy degeneracy between the valleys. The experimental results are further corroborated by an effective model, revealing distinct coupling strengths for the K and K′ valleys and a strong relation between plasmon-exciton energy detuning and valley polarization. This work offers new possibilities for information encoding and storage by exploiting the valley degree of freedom in cavity-coupled low-dimensional semiconductors.

The electronic band structure of crystals defines the dispersion relation between electrons' energy and crystal momentum. A "valley" refers to a local minimum in the conduction band or a local maximum in the valence band, introducing an additional degree of freedom for electrons beyond charge and spin[1,2]. Exploring this valley degree of freedom drives advancements in valleytronics and optoelectronics[3–5]. Group VI monolayer transition metal dichalcogenides (TMDs), with direct band gaps in the visible and near-infrared spectrum, host valley-specific interactions between circularly polarized light and excitonic states in the degenerate valence band (K and K′) due to strong spin-orbit coupling and broken inversion symmetry[6–8]. The electronic states in the K (K′) valley can be designated as valley-pseudospin up (down), providing the basis for binary information encoding through the manipulation of exciton population in either the K or K′ valleys[9].

Although valleys in TMDs hold great promise for information processing applications, the intervalley exchange interaction[10,11] and phonon-assisted scattering constitute the rapid valley depolarization[12,13], which deprives the information fidelity. In experiments, the photoluminescence (PL) from valley excitons serves as a mechanism for reading valley information, mirroring the circular polarization (CP) characteristics of incident light. Consequently, the degree of circular polarization (DCP) of the PL, defined by $\frac{I(\sigma+)-I(\sigma-)}{I(\sigma+)+I(\sigma-)}$,

[1]Department of Materials Science and Engineering, City University of Hong Kong, Hong Kong, China. [2]Department of Mechanical and Energy Engineering, Southern University of Science and Technology, Shenzhen, China. [3]Department of Physics, The Chinese University of Hong Kong, Hong Kong, China. [4]State Key Laboratory of Quantum Information Technologies and Materials, The Chinese University of Hong Kong, Hong Kong, China. [5]New Cornerstone Science Laboratory, Department of Physics, The University of Hong Kong, Hong Kong, China. [6]The Hong Kong Institute of Quantum Science & Technology, The University of Hong Kong, Hong Kong, China. [7]State Key Laboratory of Optical Quantum Materials, The University of Hong Kong, Hong Kong, China. [8]Faculties of Science and Engineering, The University of Hong Kong, Hong Kong, China. [9]Department of Physics, Centre for Functional Photonics, and Hong Kong Branch of National Precious Metals Material Engineering Research Centre, City University of Hong Kong, Hong Kong, China. e-mail: dangylei@cityu.edu.hk

can represent the degree of valley polarization. However, the depolarization induced by intervalley interactions substantially deprives the DCP of PL, posing a challenge for valley-based applications.

Metallic nanostructures act as versatile nano-optical resonators that generate intense subwavelength fields via surface plasmon (SP) excitation[14]. Various nanostructures-including single chiral nanoparticles[15], metallic gratings[16], and plasmonic gap modes[17–20]-have been used to enhance the PL DCP of monolayer TMDs. The enhanced DCP is typically attributed to the chiral Purcell effect[21] and plasmonic enhancement[15,17–20]. Nevertheless, the existing methods shorten the valley lifetime, which poses a new obstacle towards valleytronic applications.

When the coherent energy exchange rate between a quantum emitter and an optical cavity is sufficiently larger than their respective damping rate, they enter the strong coupling regime, forming exciton polaritons with extraordinary properties[22,23]. Strong coupling has been demonstrated in various systems and shows potential for maintaining the valley polarization[24,25], but the depolarization is still dominant due to degenerate energy branches in the two valleys since the coupling is not valley-specific. Therefore, a deeper understanding of selective coupling between chiral nanostructures and valley excitons is needed. Recently, bottom-up synthetic methods have enabled scalable fabrication of three-dimensional chiral nanoparticles[26], notably gold nanohelicoids (GNHs). These nanoparticles, featuring highly twisted structures with deep, narrow gaps, significantly enhance local electromagnetic fields and support high-order plasmonic modes. Their intrinsic chiral optical properties in both absorption and emission, along with a straightforward aqueous seed-mediated synthesis guided by amino acids or peptides, simplify chirality control compared to nanoscale-patterned metasurfaces[27–30]. Consequently, GNHs offer a promising platform to investigate microscopic and dynamic processes under valley-selective strong coupling conditions.

In this work, we report a prolonged valley lifetime and giant valley energy splitting of monolayer MoS_2 in a chiral plasmon-valley exciton coupling system and explore the dynamic nature using time-integrated and transient spectroscopies. The chiral plasmonic GNHs were designed and synthesized to exhibit strong circular absorption and emission contrast near the A-exciton energy of MoS_2. In the GNH-coupled system, energy splitting was observed in the scattering spectra, and PL measurements showed an increase in DCP accompanied by a valley splitting of 19 meV. Transient reflectivity (TR) measurements and electron dynamic calculations reveal that this PL DCP enhancement stems from a significantly prolonged valley exciton density contrast lifetime as well as giant valley splitting in the coupled MoS_2. Moreover, our theoretical calculations quantify the selective coupling strengths and assess the chiral cavity's influence on the two valleys in detail. These results validate a selective coupling mechanism that enhances valley polarization and deepen our understanding of plasmon-coupled valley exciton behavior.

Results

Selective strong coupling system of a GNH and monolayer MoS_2

The selectively coupled system is composed of a single GNH (diameter ~ 140 nm) placed on top of monolayer MoS_2, as shown in Fig. 1a. The MoS_2 monolayer was mechanically exfoliated from synthetic bulk crystals onto PDMS stamps, and then dry-transferred onto SiO_2/Si substrates (with SiO_2 thickness of 200 nm). Subsequently, the GNHs were drop-casted onto the monolayer MoS_2. The intrinsic helicoid structure of GNHs shown in Fig. 1a inset is a favorable prospect for chiral optical manipulations. As shown in Fig. S1a, our synthesized GNHs possess both high circular dichroism (CD) and absorption around the A-exciton energy of monolayer MoS_2. Moreover, the electric field distribution in Fig. S1b demonstrates the localized and chiral patterns when subjected to illumination by circularly polarized light (CPL).

In such a plasmon-exciton coupling system where both modes possess spin or pseudospin selectivity, the coupling effect is particularly intriguing. As shown in Fig. 1b, the chiral SP mode establishes a one-to-one correspondence with the spin state of incident photons, and can selectively couple with excitons carrying the identical pseudospin direction within a specific valley. Specifically, when the coupled system is excited with right-handed circularly polarized (RCP, similarly LCP for left-handed case) light, the right-handed GNH with the chiral plasmonic mode in correspondence to spin-up photons selectively couples with the valley-pseudospin-up excitons in the K valley of monolayer MoS_2. Despite the intervalley interactions, the selective coupling leads to a higher carrier density in the K valley than that in the K′ valley, resulting in the observed strongly $\sigma+$ polarized emission. In contrast, the intervalley interactions result in nearly equal static valley exciton densities and emission for the off-GNH pristine monolayer MoS_2, shown in Fig. S5.

To explore the coupling, we analyzed the dark-field scattering spectra and characterized the induced energy splitting. Figure 1c shows the energy branches in the scattering spectra (Fig. S8) as a function of the energy difference (detuning) between the SP resonance mode E_p and the exciton mode E_0. When the number of excitons interacting with a cavity surpasses the quantum threshold associated with the cavity mode volume, the plasmon-exciton coupling mechanism can be effectively described by the coupled-oscillator model (COM)[31] to characterize our measured energy splitting in the scattering spectra. Numerous studies have validated the reliability of the COM in depicting static plasmon-exciton coupling phenomena[23,32,33]. The Hamiltonian of coupled oscillators for one SP mode with an excitonic state can be expressed as:

$$\begin{pmatrix} E_p - i\frac{\gamma_p}{2} & g \\ g & E_0 - i\frac{\gamma_0}{2} \end{pmatrix} \begin{pmatrix} \alpha \\ \beta \end{pmatrix} = E \begin{pmatrix} \alpha \\ \beta \end{pmatrix} \quad (1)$$

where E_p, E_0 are the energies of the SP mode and the A-exciton of the monolayer MoS_2, and γ_p, γ_0 are their corresponding damping rates. α and β are the eigenvector components that represent the fraction of mixing states in this hybrid system. However, the helicoid structure of the GNHs produces multiple SP modes due to the complex surface, which appear as broad hybrid peaks in the scattering spectra. Here, we focused on a narrow spectral region around the coupling dip and approximated the involved SP mode as a single Lorentzian mode. The experimental energies of the upper and lower polariton branches (UPB and LPB) were obtained by fitting the scattering spectra of multiple single-particle GNHs with two Lorentzian peaks corresponding to varying plasmon resonance energies.

Following the mode splitting induced by the coupling effect, PL spectra of the system were investigated to verify the valley polarization enhancement. As illustrated in Fig. 1d, the coupling system exhibits a DCP value of 41.8%, significantly higher than 4.1% observed in the off-GNH case (Fig. S5). The full width at half maximum (FWHM) of the PL spectra increases from ~ 90 meV to ~ 150 meV, accompanied by different peak red-shifts for $\sigma+$ and $\sigma-$ components of emission. This indicates a line-width broadening effect and the emergence of lower polariton emission due to excitonic state splitting, which will be further discussed.

Valley-specific dynamics by transient reflectivity

The observed valley polarization enhancement can be further explained through CP-resolved TR spectroscopy, which monitors the change in valley exciton densities over time. Figure 2a, b display the decay dynamics of uncoupled and coupled valley excitons in monolayer MoS_2 pumped by $\sigma+$ light, respectively. The green connected dots stand for the exciton density in the K valley probed by $\sigma+$ light, and the red connected dots stand for that in the K′ valley probed by $\sigma-$ light. Compared to the uncoupled case, the coupled system shows

https://doi.org/10.1038/s41467-026-70544-7

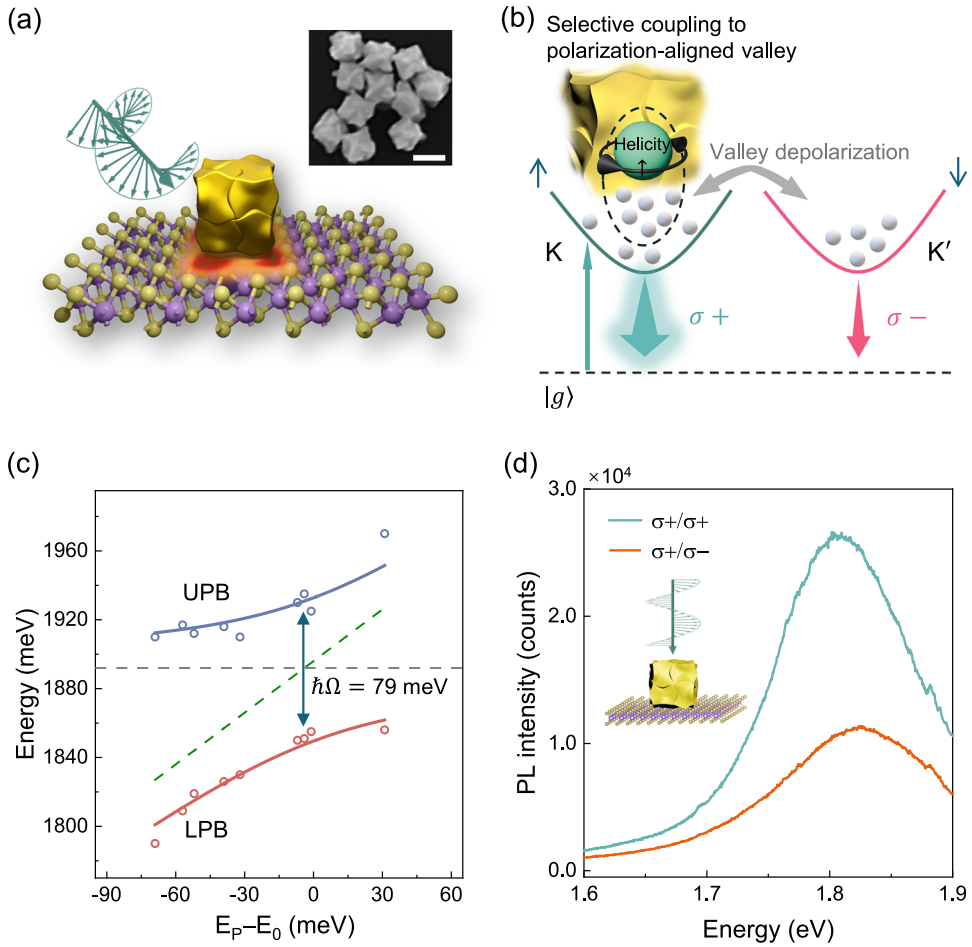

Fig. 1 | Selective coupling of a single GNH and monolayer MoS_2. a Illustration of a single GNH coupled to MoS_2 monolayer. The orange-red pattern at the GNH-MoS_2 interface indicates the plasmonic electric near-field distribution in the chiral GNH under RCP illumination. The top-right inset shows an SEM micrograph of the GNHs used in our experiments, with a scale bar of 150 nm. **b** Schematics of a chiral plasmon-valley exciton coupling system, where the chiral plasmonic mode corresponding to helicity-up photons (green sphere) in the GNH selectively couples with excitons in the K valley of MoS_2, resulting in a higher exciton density under RCP excitation, despite the valley depolarization (grey arrow). **c** Energies of UPB (blue) and LPB (red) for the GNH-MoS_2 coupling system as a function of the energy detuning between the GNH SP mode E_p and the MoS_2 A-exciton E_0. The solid curves are calculated by the coupled oscillator model with energy splitting of $\hbar\Omega = 79$ meV. The black dashed line shows the energy of the exciton mode. The green dashed line shows the energies of the GNH SP mode E_p. **d** CP-resolved PL spectra of the plasmon-exciton coupling system under illumination by an RCP ($\sigma+$) laser at 1.96 eV. The green and red curves indicate the RCP and LCP ($\sigma-$) components of the emission, respectively.

modulated decay rates (details in Fig. S10) and a remarkable valley contrast when probed with light of opposite helicities. Moreover, the overall TR signal intensity of the GNH-coupled system is also enhanced. As shown in Fig. S9, the TR signal for the $\sigma+$ ($\sigma-$) probe is enlarged by about 7 (4) folds in the first few picoseconds under the same pump-probe condition, which means the chiral plasmonic resonator boosts the circular contrast of the optical response of monolayer MoS_2.

In order to get a deeper insight into the coupling phenomena, we propose the valley-selective strong coupling model combined with the experiment data to calculate the decay dynamics in the two valleys. The total Hamiltonian in our model can be expressed as:

$$\begin{aligned} H_T &= H_0 + H_{ex} + H_c + V \\ &= \hbar \sum_{i,\tau} \left(\omega_{i,\tau} B^\dagger_{i,\tau} B_{i,\tau} + \omega'_{i,\tau} D^\dagger_{i,\tau} D_{i,\tau} \right) \\ &\quad + \sum_{i,j} \sum_{\tau,\tau'} M^{ex}_{i,j,\tau,\tau'} B^\dagger_{i,\tau} B_{j,\tau'} + \sum_{\tau} \hbar \omega_\tau a^\dagger_\tau a_\tau \\ &\quad + \hbar \sum_{\tau} g_\tau \left(B^\dagger_{A,\tau} a_\tau + B_{A,\tau} a^\dagger_\tau \right). \end{aligned} \tag{2}$$

Here, H_0, H_{ex}, H_c and V stand for the Hamiltonian of the excitons, exchange interactions, cavity, and exciton-cavity interactions, respectively. The subscript $i = A, B$ represents different excitonic states; in our framework, we consider only the 1s state of A- and B-excitons. The subscript $\tau = \pm 1$ is the valley index, where $\tau = 1$ corresponds to excitons in the K valley and $\tau = -1$ corresponds to excitons in the K′ valley. The operators $B^\dagger_{i,\tau}(D^\dagger_{i,\tau})$ represent the annihilation of bright (dark) excitons, while $B_{i,\tau}(D_{i,\tau})$ represent the creation of bright (dark) excitons. The symbols $\omega_{i,\tau}(\omega'_{i,\tau})$ denote the angular frequencies of the respective excitons. The first term corresponds to the intrinsic energy of the excitons, and the second term represents the electron-hole exchange interaction, details of which for the exchange elements $M^{ex}_{i,j,\tau,\tau'}$ can be found in the Supplementary Information (SI) Section II Part A. The third term is the energy of the optical cavity, with $a^\dagger_\tau(a_\tau)$ being the creation (annihilation) operator of photons with polarization τ. The fourth term involves the interaction between photons and excitons, considering the rotating wave approximation (RWA), where g_τ is the coupling strength between photons and τ-valley excitons.

Based on the total Hamiltonian, the corresponding decay dynamics can be theoretically derived by considering this open system's evolution as a Markov process and obtaining the Lindblad

https://doi.org/10.1038/s41467-026-70544-7

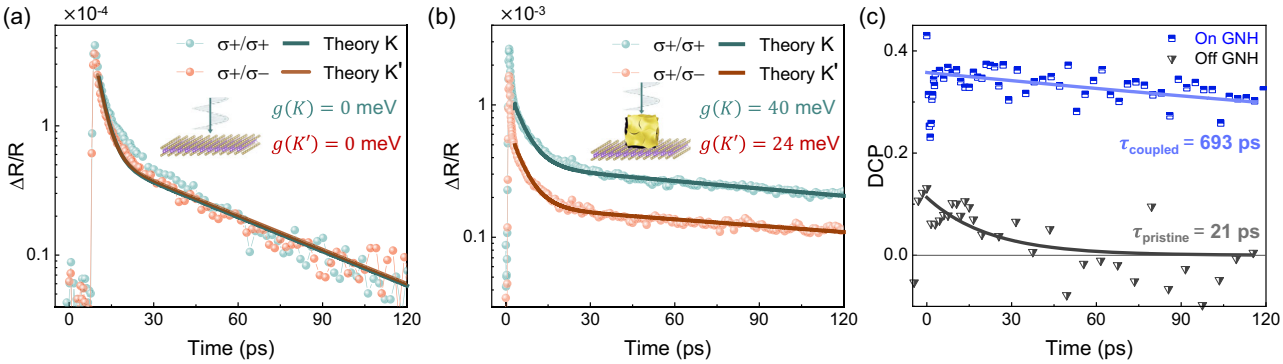

Fig. 2 | Ultrafast characterization of the valley depolarization process. Decay dynamics of the A-exciton measured at **a** off-GNH and **b** on-GNH MoS_2 monolayer, probed with RCP ($\sigma+$, green) and LCP ($\sigma-$, red) laser. The bold solid curves in **a** and **b** indicate calculated decay dynamics of the A-exciton in the K (dark green) and K′ (dark red) valleys based on our theoretical model. The valley-selective coupling strength g(K) and g(K′) are the parameters applied in our calculations. **c** DCP evolution over time. Scatter points: time-resolved DCP of the valley A-exciton density extracted from the measured decay dynamics in **a** and **b**. The solid curves are fitting results using the exponential decay function.

master equation using standard methods (SI Section II Part D)[34]. The decay dynamics measured in Fig. 2a, b can be roughly attributed to three processes, with the lifetimes of τ_1, τ_2, and τ_3 from short to long, corresponding to surface defect trapping, electron-phonon scattering, and direct electron-hole recombination, respectively (SI Section I Part D). The calculated decay dynamics of each valley are shown as solid curves in Fig. 2. We start from 3 ps after the excitons are pumped in our calculations, so the shortest τ_1 is not considered. The τ_2 and τ_3 for both uncoupled and coupled cases are set as 6 ps and 40 ps, respectively. The values are determined by referring to the exponential fitting parameters obtained in Fig. S10a. As we introduce the strong coupling effect (coupling strengths: g(K) = 40 meV, g(K′) = 24 meV, referring to the energy splitting) to the coupled case, the calculated curves by theory are consistent with the experiment data. This also proves that the prolonged τ_3 in our system originates from strong coupling[35].

We evaluate the exciton distribution and valley polarization dynamics in the coupled system, revealing the robustness of the PL DCP and its origin. Specifically, the DCP for exciton densities, calculated as $\frac{r(\sigma+)-r(\sigma-)}{r(\sigma+)+r(\sigma-)}$, is used to quantify the valley exciton distribution over time. As shown in Fig. 2c, the exciton density difference of GNH-coupled MoS_2 is maintained at DCP of ~0.35 for over 120 ps regardless of the intervalley interactions at room temperature. We apply an exponential decay function to extract the valley polarization lifetimes[36], showing an extension from 21 ps (off-GNH case) to 693 ps (on-GNH case). Theoretical calculations further indicate that the valley exciton density contrast in the coupled system persists for over a nanosecond (Fig. S9), whereas in pristine monolayer MoS_2, it drops to near zero within hundreds of femtoseconds. The prolonged lifetime of the valley excitons and their density contrast indicate that the enhanced valley polarization arises from selective strong coupling with the nano-resonator. Our experimental observations, including the energy splitting and the ultrafast dynamics, are well-explained in theory under the strong coupling regime.

The strict criterion for strong coupling is determined by the energy splitting (coupling strength) and the loss rate of the system[37]. When $E_p = E_0$, the Rabi splitting energy $\hbar\Omega = \sqrt{4g^2 - (\gamma_0 - \gamma_p)^2}/4$ is obtained from Eq. (1)[38]. In our work, the Rabi splitting of $\hbar\Omega \approx 79$ meV is observed, and the damping rate of the SP mode that couples with the exciton is $\gamma_p \approx 174$ meV. The system has not reached the strict criterion of $\hbar\Omega > (\gamma_0 + \gamma_p)/2$ according to the far-field scattering measurements. The helicoid surface structure of the GNH is responsible for the measured wide hybrid peak, leading to the broadening of the SP mode and a larger γ_p. The observed splitting and anticrossing between the two energy branches suggest the strong coupling effect in the near field and help us better understand the nature of our CP-resolved time-integrated PL and ultrafast decay dynamics experiments.

Mode-dependent enhancement and distribution of local optical chirality

The near-field optical chirality of the GNH structure is analyzed through simulations to elucidate the strong coupling phenomenon. The superchiral field and its interaction with light are quantified using the concept of local optical chirality[28,39,40]. Derived as a pseudoscalar based on time and parity symmetry, the near-field distribution of optical chirality is expressed as $C(\boldsymbol{r}) = -\frac{\varepsilon_0\omega}{2}\mathrm{Im}[\boldsymbol{E}^*(\boldsymbol{r})\cdot\boldsymbol{B}(\boldsymbol{r})]$, where ε_0, ω, $\boldsymbol{E}$ and $\boldsymbol{B}$ are the permittivity of the vacuum, angular frequency, electric field and magnetic flux density, respectively. This term has been interpreted as an intrinsic physical quantity that can be transferred (dissipated) to discrete objects[41], which can account for the observed selective coupling between the GNH and MoS_2.

The integration of the optical chirality enhancement C/C_0 at different wavelengths is calculated and plotted as red connected dots in Fig. 3a, where C_0 is the optical chirality of circularly polarized light without the presence of the GNH. The spatial distributions of optical chirality at different wavelengths are plotted in Fig. 3b, d, showing highly energy-dependent properties in the near field. The plasmon resonance mode corresponding to Fig. 3d demonstrates strong and localized optical chirality, with the energy ideal for coupling with valley excitons in monolayer MoS_2. The unique helicoid surface structure provides optimal conditions for selective coupling.

Valley energy splitting induced by selective Rabi splitting

The lower polariton emission often dominates the PL in the strong coupling regime due to energy relaxation and dynamic population transfer, favoring the lower energy branch[42,43]. As the selective coupling inflicts different coupling strengths on the two valleys, it should also result in different energy splittings. We measured the CP-resolved PL spectra of pristine monolayer MoS_2 and GNH-MoS_2 coupling systems with different DCP enhancement. The PL spectra can be considered as the combined emission from the lower polariton and the pristine A-exciton, and the components are recognized via two Lorentzian fittings. As shown in Fig. 4a, the lower-polariton emission (green fits; bottom three panels) exhibits a pronounced polarization- and sample-dependent energy shift: the redshift varies not only among different samples with different PL DCP, but also between the K and K′ valley emissions within the same sample. This behavior is consistent with valley-selective strong coupling, which induces different polariton splittings and therefore different lower-polariton energies. By

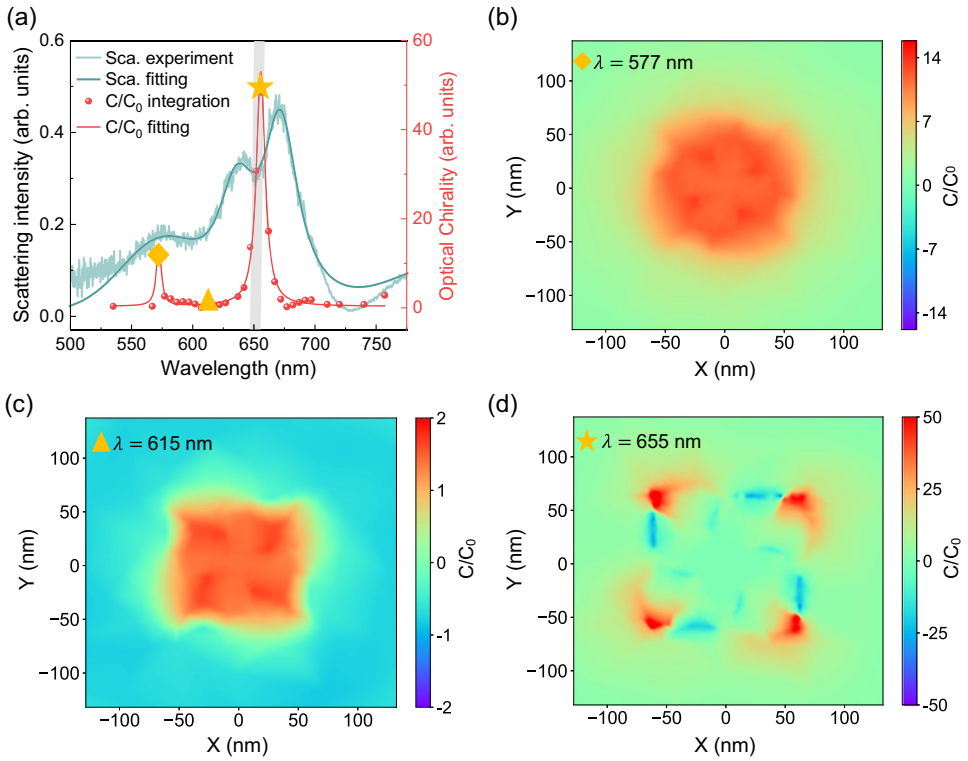

Fig. 3 | Optical chirality enhancement and localization. a Dark-field scattering spectrum of a GNH-MoS_2 coupling system, fitted with Lorentzian functions (green curves). Red dots show the wavelength-dependent integrated optical chirality enhancement C/C_0, also fitted with Lorentzian functions. The gray shaded band marks the A-exciton energy of monolayer MoS_2. (**b**–**d**) Local optical chirality enhancement (C/C_0) distributions calculated at 577, 615 and 655 nm, respectively.

contrast, the A-exciton emission (gray fits) remains unchanged across polarizations and samples, as it is affected by the Purcell effect in the weak coupling regime.

The mechanism can be illustrated by Fig. 4b, in which stronger coupling is induced in the K valley, and as a result, the LPB of the K valley is lower than that of the K′ valley. The relation between the valley splitting and PL DCP is plotted in Fig. 4c with a linear dependence, where the largest splitting of 19.6 meV between the two valleys is achieved. The error bars represent the Lorenzian fitting errors. In previous studies, such a giant valley splitting can be realized by applying an external magnetic field as large as 60 T[44] or a smaller magnetic field with magnetic proximity effect[45]. In our work, we demonstrate such a significant breaking of the energy degeneracy of K and K′ valleys by plasmon-exciton selective strong coupling.

Another important degree of freedom in this system is the resonance detuning between the SP mode and the exciton. The inset of Fig. 4c compares experimentally measured DCP from GNH-MoS_2 systems across various SP modes (green dots) to theoretical predictions from exciton population dynamics (Fig. S13), adjusted by a linear correction factor. Remarkably, reducing the energy detuning from 69 to 1 meV significantly increases DCP from 0.12 to 0.42 and enhances PL intensity fourfold, identifying DCP as an important energy-detuning-dependent parameter.

Discussion

Our results chart a practical path to ambient-condition valleytronics by co-realizing a field-free giant K/K′ splitting and a markedly extended valley depolarization time in a single-particle chiral plasmon-exciton platform. The longer depolarization time directly translates into more durable retention of valley pseudospin information, while detuning provides an efficient lever for controlling PL intensity and DCP-enabling compact, energy-efficient valley gating and routing without cryogenics or magnetic fields. This co-realization surpasses weak-coupling or purely dielectric strategies that either accelerate decay or leave K/K′ degenerate[15,17–21], and rivals magnetic approaches in magnitude[44,45] while remaining on-chip. These findings reveal chiral, frequency-locked read-out with effective brightening, which could enable robust pseudospin memory, valley-addressable modulators, and low-threshold valley-polarized emitters under ambient conditions.

In summary, we have demonstrated valley-selective strong coupling between the chiral plasmonic resonances of the GNH and valley excitons in monolayer MoS_2. This coupling gives rise to two central findings: a pronounced valley energy splitting of approximately 19 meV and a significantly prolonged valley lifetime, experimentally confirmed through steady-state PL and time-resolved TR measurements. Supporting calculations reveal asymmetric coupling strengths to the K and K′ valleys and clarify the role of localized chiral near fields in lifting valley degeneracy and stabilizing valley exciton population imbalance. These results provide a compelling route towards dynamic and room-temperature control of valley-polarized emission in 2D semiconductors via chiral nanophotonics, presenting a novel perspective for analyzing plasmon-exciton coupling in the field of valleytronics in TMDs.

Methods

Sample preparation

Helical Au nanoparticles were synthesized via a modified seed-mediated protocol adapted from Lee et al.[26]. Briefly, Au seeds were produced by $NaBH_4$ reduction of $HAuCl_4$ in cetrimonium bromide (CTAB), diluted, and used to grow CTAB-stabilized cubic seeds. Helical growth was then performed in a CTAB/$HAuCl_4$/amino-acid solution, initiated by L-glutathione and the cubic seeds, followed by incubation at 30 °C for ~ 2 h; products were purified by centrifugation and redispersed in 1 mM CTAB. During the synthesis, the seed size, amino-

https://doi.org/10.1038/s41467-026-70544-7

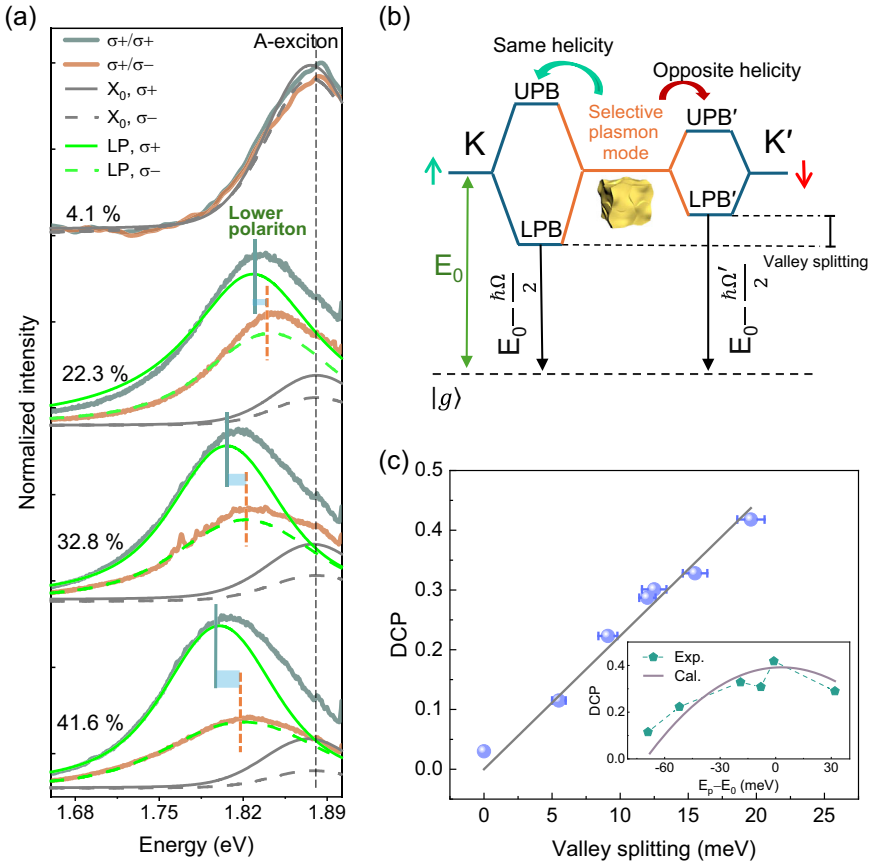

Fig. 4 | Correlation of PL DCP and energy splitting between two valleys. a CP-resolved PL spectra of pristine monolayer MoS_2 (top panel, with one Lorenzian fitting of A-exciton) and GNH-MoS_2 coupling systems (bottom three panels, with two Lorenzian fittings of the lower polariton (green) and A-exciton (black)) with increasing valley splitting. The solid and dashed fitting curves are the components for $\sigma+$ and $\sigma-$ emissions, respectively. The increasing energy splitting across samples is achieved by increasing the centrifugation time from 120 s to 180 s to adjust the distance between the GNH and monolayer MoS_2, as described in the Methods. **b** Schematics of valley splitting induced by the valley-selective coupling effect. The plasmon mode of the right-handed GNH is of the same helicity as the excitonic state in the K valley and generates a larger energy splitting, compared to that of the K′ valley. **c** Correlation of the PL DCP and the valley splitting. The blue dots are extracted from experiments (error bars represent Lorenzian fitting errors), and the dark line is a linear fit. Inset: PL DCP as a function of energy detuning. The green dots are measured DCP, and the purple curve is extracted from theoretical calculations.

acid concentration, and growth time were adjusted to tune the plasmonic resonance and circular dichroism near the MoS_2 A-exciton. Full reagent concentrations and volumes are provided in the SI Section I Part A.

Monolayer MoS_2 was prepared by mechanically exfoliating bulk MoS_2 crystals (HQ Graphene) using the standard "Scotch tape" method. Briefly, a small piece of bulk crystal was placed on adhesive tape, which was then repeatedly folded and peeled to thin from the flakes. The tape was subsequently pressed onto a clean polydimethylsiloxane (PDMS) film and swiftly peeled off, leaving monolayers of MoS_2 on the surface of the PDMS stamp. Eventually, the PDMS stamp was carefully pressed onto a Si substrate coated with 200 nm of SiO_2 and peeled off. The resulting MoS_2 monolayers on the Si substrate were first identified under an optical microscope and subsequently verified using fluorescence and Raman microspectroscopy.

The as-synthesized GNH solution was diluted with deionized water (1:80), centrifuged at 350 g for 120-180 s, and the supernatant was removed. The centrifugation time was varied to control the thickness of the CTAB layer on GNHs, with longer times resulting in a reduced GNH-MoS_2 distance in the final sample. The precipitate was redispersed in deionized water (1:40), sonicated for 8 min to ensure single-particle dispersion, and finally aqueous dispersions of GNHs were drop-casted onto the MoS_2 monolayers to construct the coupled system.

Optical measurements

The GNHs were first evenly dispersed in water using ultrasonic vibration, and their absorption and circular dichroism (CD) spectra were then measured with a JASCO J-1500 CD Spectrometer. The microscopic dark-field scattering, Raman scattering, photoluminescence (PL), and transient reflectivity (TR) spectra were measured using a home-built polarization-resolved microscopic system. The microscopic system was customized based on an Olympus BX51 upright fluorescence microscope with additional non-polarizing modules and half-waveplates (AHWP05M-580, THORLABS) to ensure minimal polarization distortion induced by the beam splitters. The optical signal was collected with an objective lens (Olympus MPlan 100 ×/0.80 BD) and analyzed through a monochrometer (Andor SR-500i) directly through a free-space light setup.

TR measurements were carried out using a custom-built narrowband microscopic TR setup equipped with computer-controlled Galvo mirrors to ensure precise spatial overlap between the tightly focused pump and probe beams. Ultrafast laser pulses were provided by a Coherent Chameleon Ultra II Ti:sapphire laser system, delivering 140 fs pulses at an 80 MHz repetition rate. The fundamental output was coupled into an optical parametric oscillator (OPO) to generate tunable probe wavelengths. In the present measurements, photon energies of 2.85 eV and 1.85 eV were selected for the pump and probe beams, respectively. The system enables valley addressability and

temporal resolution of exciton dynamics in the studied monolayer samples, with the pump-probe delay controlled by a motorized optical delay line. The pump and probe beams were first guided with high-precision galvo lens for spatial overlap and then tightly focused by the objective lens (Olympus MPlan 100 × /0.80 BD) to a spot size of $0.8\,\mu m^2$, with power fluences of $8\,\mu J/cm^2$ and $0.8\,\mu J/cm^2$, respectively. (Fig. 2).

Theoretical calculations

We model the monolayer TMD coupled to a chiral single-mode cavity using a minimal exciton-photon Hamiltonian that includes bright/dark A,B excitons in both valleys and their long-range electron-hole exchange (full matrices in SI). Light-matter coupling is valley-selective (RCP → K, LCP → K′) and treated within the rotating-wave approximation; in the final model only the A-exciton couples to the cavity mode, the cavity's chirality enters through unequal couplings ($g_{+1} \neq g_{-1}$):

$$V = \hbar \sum_{\tau = \pm 1} g_\tau \left(B^\dagger_{A,\tau} a_\tau + B_{A,\tau} a^\dagger_\tau \right). \tag{3}$$

Dissipation and bright ↔ dark interconversion are captured by a secular Lindblad master equation with radiative decay and chiral-phonon-assisted spin flips,

$$\dot{\rho} = -\frac{i}{\hbar}[H_T, \rho] + \mathbb{L}\rho, \tag{4}$$

where $\mathbb{L}$ is the Lindblad superoperator. Numerical spectra for TR are obtained from the third-order response in the short-pulse/dipole limit by propagating populations with the rate matrix extracted from the Liouvillian. For calculation details, all parameters used in simulations and the explicit exchange blocks are listed in Section II of the Supplementary.

Data availability

The collected data that support the findings of this study are available upon request from the corresponding author (D.L.).

References

1. Rycerz, A., Tworzydło, J. & Beenakker, C. Valley filter and valley valve in graphene. *Nat. Phys.* **3**, 172–175 (2007).
2. Shkolnikov, Y., De Poortere, E., Tutuc, E. & Shayegan, M. Valley splitting of AlAs two-dimensional electrons in a perpendicular magnetic field. *Phys. Rev. Lett.* **89**, 226805 (2002).
3. Gunawan, O. et al. Valley susceptibility of an interacting two-dimensional electron system. *Phys. Rev. Lett.* **97**, 186404 (2006).
4. Xiao, D., Liu, G.-B., Feng, W., Xu, X. & Yao, W. Coupled spin and valley physics in monolayers of MoS_2 and other group-VI dichalcogenides. *Phys. Rev. Lett.* **108**, 196802 (2012).
5. Schaibley, J. R. et al. Valleytronics in 2D materials. *Nat. Rev. Mater.* **1**, 1–15 (2016).
6. Mak, K. F., McGill, K. L., Park, J. & McEuen, P. L. The valley Hall effect in MoS_2 transistors. *Science* **344**, 1489–1492 (2014).
7. Zhu, Z. Y., Cheng, Y. C. & Schwingenschlögl, U. Giant spin-orbit-induced spin splitting in two-dimensional transition-metal dichalcogenide semiconductors. *Phys. Rev. B: Condens. Matter Mater. Phys.* **84**, 153402 (2011).
8. Aivazian, G. et al. Magnetic control of valley pseudospin in monolayer WSe_2. *Nat. Phys.* **11**, 148–152 (2015).
9. Gedik, N. Valley-selective optical stark effect in monolayer WS_2. In *APS Mar. Meet. Abstr.*, vol. 2016, X17–004 (2016).
10. Yu, H., Liu, G.-B., Gong, P., Xu, X. & Yao, W. Dirac cones and Dirac saddle points of bright excitons in monolayer transition metal dichalcogenides. *Nat. Commun.* **5**, 3876 (2014).
11. Glazov, M. M. et al. Exciton fine structure and spin decoherence in monolayers of transition metal dichalcogenides. *Phys. Rev. B* **89**, 201302 (2014).
12. Jones, A. M. et al. Optical generation of excitonic valley coherence in monolayer WSe_2. *Nat. Nanotechnol.* **8**, 634–638 (2013).
13. Hao, K. et al. Direct measurement of exciton valley coherence in monolayer WSe_2. *Nat. Phys.* **12**, 677–682 (2016).
14. Lei, D. Y. et al. Revealing plasmonic gap modes in particle-on-film systems using dark-field spectroscopy. *ACS Nano* **6**, 1380–1386 (2012).
15. Kim, S. et al. A single chiral nanoparticle induced valley polarization enhancement. *Small* **16**, 2003005 (2020).
16. Zhao, L.-Y. et al. Ultrafast modulation of valley dynamics in multiple WS_2- Ag gratings strong coupling system. *PhotoniX* **3**, 5 (2022).
17. Li, Z. et al. Tailoring MoS_2 valley-polarized photoluminescence with super chiral near-field. *Adv. Mater.* **30**, 1801908 (2018).
18. Sun, J., Hu, H., Pan, D., Zhang, S. & Xu, H. Selectively depopulating valley-polarized excitons in monolayer MoS_2 by local chirality in single plasmonic nanocavity. *Nano Lett.* **20**, 4953–4959 (2020).
19. Wen, T. et al. Steering valley-polarized emission of monolayer MoS_2 sandwiched in plasmonic antennas. *Sci. Adv.* **6**, eaao0019 (2020).
20. Lin, W.-H. et al. Electrically tunable and dramatically enhanced valley-polarized emission of monolayer WS_2 at room temperature with plasmonic archimedes spiral nanostructures. *Adv. Mater.* **34**, 2104863 (2022).
21. Yoo, S. & Park, Q.-H. Chiral light-matter interaction in optical resonators. *Phys. Rev. Lett.* **114**, 203003 (2015).
22. Schneider, C., Glazov, M. M., Korn, T., Höfling, S. & Urbaszek, B. Two-dimensional semiconductors in the regime of strong light-matter coupling. *Nat. Commun.* **9**, 2695 (2018).
23. Niu, Y., Xu, H. & Wei, H. Unified scattering and photoluminescence spectra for strong plasmon-exciton coupling. *Phys. Rev. Lett.* **128**, 167402 (2022).
24. Sun, Z. et al. Optical control of room-temperature valley polaritons. *Nat. Photonics* **11**, 491–496 (2017).
25. Liu, X. et al. Nonlinear valley phonon scattering under the strong coupling regime. *Nat. Mater.* **20**, 1210–1215 (2021).
26. Lee, H.-E. et al. Amino-acid-and peptide-directed synthesis of chiral plasmonic gold nanoparticles. *Nature* **556**, 360–365 (2018).
27. Karst, J. et al. Chiral scatterometry on chemically synthesized single plasmonic nanoparticles. *ACS Nano* **13**, 8659–8668 (2019).
28. Gao, H., Chen, P.-G., Lo, T. W., Jin, W. & Lei, D. Selective excitation of polarization-steered chiral photoluminescence in single plasmonic nanohelicoids. *Adv. Funct. Mater.* **31**, 2101502 (2021).
29. Chen, P. et al. Chiral coupling of valley excitons and light through photonic spin–orbit interactions. *Adv. Opt. Mater.* **8**, 1901233 (2020).
30. Chen, P.-G., Lo, T. W. & Lei, D. Breaking the mirror symmetry of photonic spin-orbit interaction using a geometrically symmetric chiral resonator. *J. Opt.* **26**, 07LT01 (2024).
31. Chikkaraddy, R. et al. Single-molecule strong coupling at room temperature in plasmonic nanocavities. *Nature* **535**, 127–130 (2016).
32. Lo, T. W. et al. Thermal redistribution of exciton population in monolayer transition metal dichalcogenides probed with plasmon–exciton coupling spectroscopy. *ACS Photonics* **6**, 411–421 (2019).
33. Cuadra, J. et al. Observation of tunable charged exciton polaritons in hybrid monolayer WS_2- plasmonic nanoantenna system. *Nano Lett.* **18**, 1777–1785 (2018).
34. Agarwal, G. S.*Quantum Opt*. (Cambridge University Press, 2012).
35. Koshelev, K., Sychev, S., Sadrieva, Z. F., Bogdanov, A. A. & Iorsh, I. Strong coupling between excitons in transition metal dichalcogenides and optical bound states in the continuum. *Phys. Rev. B* **98**, 161113 (2018).

36. Koutensky`, P. et al. Ultrafast dynamics of valley-polarized excitons in wse2 monolayer studied by few-cycle laser pulses. *Nanomaterials* **13**, 1207 (2023).
37. Dovzhenko, D., Ryabchuk, S., Rakovich, Y. P. & Nabiev, I. Light–matter interaction in the strong coupling regime: configurations, conditions, and applications. *Nanoscale* **10**, 3589–3605 (2018).
38. Wu, Q. et al. Strong coupling of excitons in monolayer WS_2 with guided-mode resonance. *Results Phys.* **44**, 106191 (2023).
39. Tang, Y. & Cohen, A. E. Optical chirality and its interaction with matter. *Phys. Rev. Lett.* **104**, 163901 (2010).
40. Tang, Y. & Cohen, A. E. Enhanced enantioselectivity in excitation of chiral molecules by superchiral light. *Science* **332**, 333–336 (2011).
41. Mun, J. et al. Electromagnetic chirality: from fundamentals to nontraditional chiroptical phenomena. *Light.: Sci. Appl.* **9**, 139 (2020).
42. Bisht, A. et al. Collective strong light-matter coupling in hierarchical microcavity-plasmon-exciton systems. *Nano lett.* **19**, 189–196 (2018).
43. Qiu, L. et al. Molecular polaritons generated from strong coupling between CdSe nanoplatelets and a dielectric optical cavity. *J. Phys. Chem. Lett.* **12**, 5030–5038 (2021).
44. Stier, A. V., McCreary, K. M., Jonker, B. T., Kono, J. & Crooker, S. A. Exciton diamagnetic shifts and valley Zeeman effects in monolayer WS_2 and MoS_2 to 65 Tesla. *Nat. Commun.* **7**, 10643 (2016).
45. Norden, T. et al. Giant valley splitting in monolayer WS_2 by magnetic proximity effect. *Nat. Commun.* **10**, 4163 (2019).

Acknowledgements

D.L. acknowledges the support from the Research Grants Council of Hong Kong through a General Research Fund grant (11309623), an Area of Excellence grant (AoE/P-701/20), and the City University of Hong Kong (Grant Nos. 7005945 and 9229137). W.Y. acknowledges the support from the Research Grant Council of Hong Kong (Grant Nos. AoE/P-701/20 and A-HKU705/21), and National Natural Science Foundation of China (No. 12425406). L.G. acknowledges the support from the Natural Science Foundation of Guangdong Province (Grant No. 2024B1515020077). X.Z., W.Y., and D.L. acknowledge the support from the Guangdong Provincial Quantum Science Strategic Initiative (GDZX2204004 and GDZX2304001, GDZX2304003). C.H. acknowledges the support from the start-up fund and the Direct Grant (Grant No. 4053726) of the Chinese University of Hong Kong, the National Natural Science Foundation of China (Grant No. 12504222), and the State Key Laboratory of Quantum Information Technologies and Materials. D.L. thanks Professor Yuri Kivshar from the Australian National University and Professor Xiao Li from The City University of Hong Kong for their careful proofreading and useful comments.

Author contributions

D.L., J.L., and F.L. conceived and designed the experiments. J.L., T.X., and Y.W. performed the experiments. T.X. synthesized the chiral gold nanoparticles. F.L. and J.L. performed the theoretical modeling and calculations. J.L., F.L., Z.P., C.H., and D.L. carried out the analysis. D.L., L.G., C.H., W.Y., and X.Z. supervised the project. J.L. and F.L. wrote the manuscript. D.L., L.G., C.H., W.Y., and Z.P. revised the manuscript.

Competing interests

The authors declare no competing interests.

Additional information

Supplementary information The online version contains supplementary material available at https://doi.org/10.1038/s41467-026-70544-7.

Correspondence and requests for materials should be addressed to Dangyuan Lei.

Peer review information *Nature Communications* thanks Wei-Hsiang Lin and the other, anonymous, reviewer(s) for their contribution to the peer review of this work. A peer review file is available.